Numerical modelling of the long-term cyclic response of laterally loaded piles driven in sands using the High-Cycle Accumulation framework

Authors

P. Tantivangphaisal, D. M. G. Taborda, S. Kontoe, T. Liu, R. J. Jardine

Abstract

The High-Cycle Accumulation framework is modified and coupled with a practice-oriented cyclic sand constitutive model and implemented in a geotechnical finite element software to test the approach's ability to predict the outcomes of monotonic and cyclic lateral loading field tests performed in Dunkirk, France, under the Pile-Soil Analysis (PISA) Joint Industry Project. A consistent and rational calibration procedure using only site-specific in-situ investigation and laboratory tests is presented and a single set of calibrated parameters is shown to reproduce Dunkirk sand's response in monotonic, drained cyclic and undrained cyclic triaxial element tests up to 10,000 cycles, covering a wide range of densities and stress conditions. The finite element analyses are shown to match well the monotonic lateral loading responses of fully instrumented 2m and 0.76m diameter open steel driven test piles and the latter's cyclic lateral response up to 30,000 cycles. New insights into the evolution of the ground state under long-term lateral cyclic loading are gained to inform future research into practical site-specific methods for cyclic loading design over the full lifespan of piled foundations. (176 words)

1 Introduction

The development of robust site-specific design methods to predict the long-term response of pile foundations under lateral cyclic loading is a key issue in the design of offshore wind turbine (OWT) and other structures (Abadie et al., 2023). The satisfactory performance of monopile supported OWTs (CFMS, 2020; DNV, 2021) relies crucially on avoiding lateral instability and excessive deformations under ultimate limit (ULS) and serviceability (SLS) limit state conditions. Short-term (e.g. storm) and long-term repetitive (e.g. wind and wave) loading may be critical to SLS design, while characterisation of the system stiffness (and a lifetime range of values) is required for fatigue limit state checks (Arany et al., 2017).

Models capturing pile-soil cyclic lateral loading behaviour are generally based on extending existing monotonic loading approaches. Examples are summarised in Table 1, grouped into categories of reducing modelling complexity.

Table 1 Summary of geotechnical models proposed for cyclic lateral loading of piles.

Category		References
A (most detailed)	3D continuum with 2D frictional interface between pile and soil	Achmus et al. (2009), Corciulo et al. (2017), Staubach & Wichtmann (2020), Liu et al. (2022a), Gao et al. (2023)
B	Multiple (Winkler-type) 1D springs distributed along pile length	Peralta et al. (2017), Zhang et al. (2020), Kementzetzidis et al. (2022), Williams et al. (2022), Abadie et al. (2023)
C (most approximate)	Global 1D spring(s) only at mudline level, also called '0D', 'macro-element' or 'macro-model'	Page et al. (2021), Abadie et al. (2023)

OWT monopile design now employs three dimensional (3D) finite element (FE) models (CFMS, 2020; DNV, 2021) routinely to validate simpler schemes of distributed (Winkler) or mudline-level springs. These rely on rational and robust site-specific calibration

procedures that may be checked against benchmark sets of field-scale pile tests, provided that similar conditions exist at intended project sites. The use of 3D FE analyses to model long-term cyclic behaviour at sand sites presents two main challenges:

1) Establishing constitutive models capable of reproducing critical aspects of sands' mechanical response under tens to hundreds of relatively high load level cycles and covering representative stress states, densities, stress directions and directional changes. Examples of such analyses of laterally loaded monopiles include Liu et al. (2022a), Liu & Kaynia (2023), Kheffache et al. (2023) and Li et al. (2023).

2) Considering the millions of lower loading cycles sustained over the piles' design lives. Feasible approaches for application at the FE integration point level include equivalent degraded cyclic stiffness (Achmus et al., 2009; Gao et al., 2023) and cycle-dependent strain accumulation laws (Suiker & De Borst, 2003; Niemunis et al., 2005; Pasten et al., 2014; Staubach & Wichtmann, 2020; Staubach et al., 2022a).

The High-Cycle Accumulation (HCA) framework considered in this paper can address both challenges by averaging and characterising the material point stress-strain response of soils under cyclic loading as a time-dependent phenomena, rather than incremental stress-strain constitutive relationships. While a cycle-by-cycle treatment may be more appropriate for the most severe cycles under design storm conditions, HCA can effectively evaluate the impact of a large number of regular lateral loading cycles on monopiles. The HCA framework for geotechnical FE modelling (Niemunis et al., 2005; Wichtmann et al., 2013; Staubach et al., 2022b) was developed from laboratory drained triaxial tests on clean sands covering a wide range of void ratios, average mean effective stress, average stress ratios, strain amplitudes and directions (Wichtmann, 2005). The HCA treatment extends continuum constitutive modelling by combining it with an empirical framework for geotechnical predictions involving large numbers of cycles (Galindo et al., 2014; Teng et al., 2018; Page et al., 2021; Birrell et al., 2022).

Numerical aspects of the HCA framework and its supporting laboratory evidence in sands are well established (Wichtmann et al., 2010a, 2013, 2015, 2007; Wichtmann & Knittel, 2020; Knittel et al., 2023; Staubach et al., 2022b; Wichtmann, 2016). An extension to reconstituted kaolin clay has also been proposed (Wichtmann, 2016:pp.290–299; Staubach et al., 2022a). The framework has been applied in back-analyses of monitored, field-scale geotechnical structures (Zachert et al., 2015; Machacek et al., 2018; Zachert et

al., 2020) through coupling with a hypoplastic constitutive model (von Wolffersdorff, 1996) employing intergranular strain (Niemunis & Herle, 1997). Other related HCA applications include Jostad et al. (2020) and Page et al. (2021) using hypoelastic low-cycle models and monopile studies coupled with a hypoplastic base model by Westermann et al. (2014) and Staubach & Wichtmann (2020). Staubach et al. (2024) recently extended the framework to multi-dimensional strain paths and multi-amplitude cyclic loads with comparison against laboratory scale model tests including large deformation modelling of pile installation.

However, it is not yet clear how HCA analyses can be incorporated into practical, site-specific geotechnical design for OWT monopiles or other structures. Current cyclic design practice assesses deformations typically only for the most severe tens or hundreds of loading cycles via an idealisation (e.g. rainflow counting (ASTM, 2023)) of single design storm events (Andersen et al., 2013). Benchmark cyclic laboratory datasets, such as the Karlsruhe fine sand database (Wichtmann, 2005), rather than site-specific cyclic laboratory studies, are generally employed to gauge the ground response through approximate procedures. This approach implicitly assumes similarity between sands and structures and ignores the impact of long-term loading events and other storm events.

This paper sets out a site-specific approach for predicting long-term cyclic loading at sand sites that modifies and extends the HCA framework, coupling it with a practice-oriented state-parameter based low-cycle constitutive model (Taborda et al., 2016, 2022; Tantivangphaisal et al., 2024). These changes address certain numerical instabilities and capture better the cyclic triaxial response of marine sand (Liu, 2018; Zdravkovic et al., 2020; Taborda et al., 2020). A single set of low-cycle model and high-cycle framework parameters is established from drained and undrained, monotonic and cyclic, triaxial tests on dense Dunkirk sand by Liu (2018). Numerical predictions compare well against field tests on open steel driven piles that sustained up to 30,000 lateral load cycles during the Pile-Soil Analysis (PISA) experiments at Dunkirk (Byrne et al., 2020). This paves way for the method to be further explored to inform future practical lateral cyclic design methods for offshore piles and other similarly loaded foundations.

2 Extension and modification of HCA for sands

As indicated in Figure 1, HCA finite element analyses involve switching the constitutive relationship at each integration point between conventional 'monotonic' or 'low-cycle' loading and 'accumulation' or 'high-cycle' phases (Niemunis et al., 2005). For low-cycle analysis, the general incremental stress-strain relationship is:

$$\{\Delta\sigma\}_{con} = [D^{ela}](\{\Delta\varepsilon^{tot}\} - \{\Delta\varepsilon^{pl}\}) \quad (1)$$

while during accumulation or high-cycle analysis, the above becomes:

$$\{\Delta\sigma\}_{acc} = \left[D^{ela}_{HCA}\right](\{\Delta\varepsilon^{tot}\} - \{\Delta\varepsilon^{pl}\} - \{\Delta\varepsilon^{acc}\}) \quad (2)$$

Where σ is the Cauchy stress tensor, and assuming infinitesimal strains its conjugate is ε. $[D^{ela}]$ is the tangent elastic stiffness, Δ denotes an arbitrary small incremental quantity, superscripts ^{tot}, ^{pl}, ^{acc} denote total, plastic and accumulated quantities, respectively.

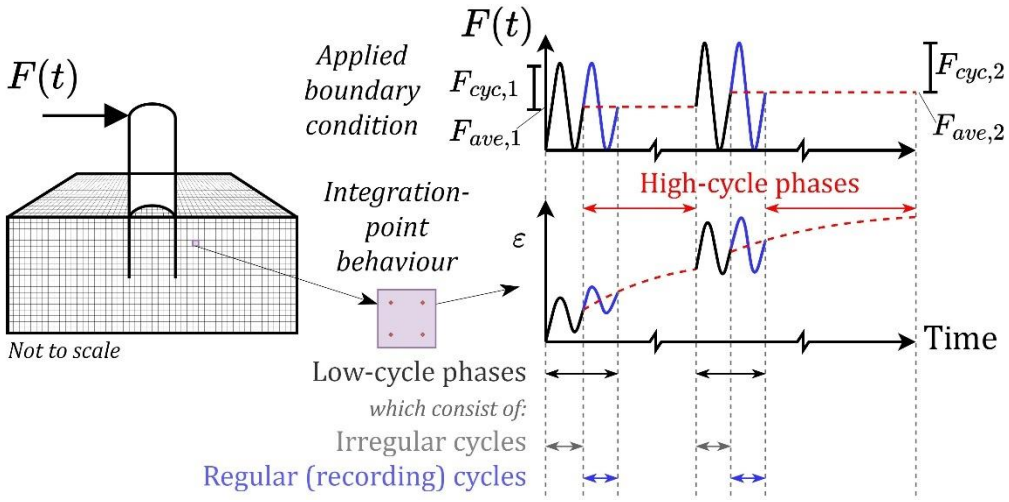


Figure 1 Illustration of the different analysis phases in an HCA FE model.

2.1 Low-cycle model

The base version of the Taborda et al. (2022) elastoplastic model consists of isotropic hypo- or non-linear elasticity with non-associated plasticity and isotropic hardening (and/or softening) based on the Mohr-Coulomb failure criterion with both yield surface and plastic flow dependent on the sand's state parameter (Been & Jefferies, 1985). The hypo-elastic tangent stiffness varies with density, stress and shear strain during cyclic loading through a strain-space reversal detection algorithm (Taborda, 2011; Taborda et

al., 2016). Implementation as a User Defined Soil Model (UDSM) in PLAXIS (Bentley Systems, 2024) is described by Taborda et al. (2023). Modularity of the implementation allows for easy incremental upgrades to the model if targeted material tests are available to inform their calibration, for example a generalised shape for the yield surface in the deviatoric plane. The base version of the model already captures the crucial influence of the sand state parameter on peak strength and plastic dilatancy. Each material parameter has a unique physical meaning and is found via a logical stepwise calibration procedure. The calibrated low-cycle model can reproduce local and global response for small numbers of loading cycles at a wide range of magnitudes. Appendix Table A-1 summarises the key equations and state variable evolution rules.

2.2 Modifications to HCA

Table 2 summarises the modifications made to the original HCA framework to match the Dunkirk laboratory tests (Liu, 2018) and achieve stability in finite element analyses. Changes to the stress ratio, void ratio and cycle number contributions to strain accumulation rate (f_Y, f_e and f_N respectively) are detailed in Tantivangphaisal et al. (2025) alongside other aspects of the numerical implementation.

134 Table 2 High-cycle accumulation equations: original and modified.

Equation		Original	Modified	Material parameters	State variables
Direction of accumulated strain increment					
(3)	$\{\vec{m}\}$	Unit vector normal to the Modified Cam Clay surface defined by ϕ'_{cs} and current average stress state $p'_{av}, J_{av}, \theta_{av}$	A calibrated ϕ'_{dir} used instead of ϕ'_{cs}	ϕ'_{dir}	$p'_{av}, J_{av}, \theta_{av}$
Cyclic history $g_{cyc} = f_{ampl} \cdot f_N; \frac{\partial g_{cyc}}{\partial N} = f_{ampl} \cdot \frac{\partial f_N}{\partial N}$					
(4)	f_{ampl}	$\min\left(\left(\frac{\varepsilon^{ampl}}{10^{-4}}\right)^{C_{ampl}}, 10^{C_{ampl}}\right)$	$\left(\frac{\min(\varepsilon^{ampl}, \varepsilon^{lim})}{10^{-4}}\right)^{C_{ampl}}$	$C_{ampl}, \varepsilon^{lim}$	ε^{ampl}
(5)	$\frac{\partial f_N}{\partial N}$	$\frac{C_{N1}C_{N2}}{(1+C_{N2}N_0)} \exp\left(\frac{g^A(N_0) - g^A(N)}{C_{N1} f_{ampl}}\right) + C_{N1}C_{N3}$	$C_{N1}C_{N2}\left(\frac{g_{cyc} - g_{cyc}(N_0)}{f_{ampl} \cdot C_{N1}} + (1+N_0)^{C_{N2}}\right)^{\left(1-\frac{1}{C_{N2}}\right)}$	C_{N1}, C_{N2}	g_{cyc}, $g_{cyc}(N_0), N_0$
Void ratio, mean effective stress and normalised stress ratio dependent factors					
(6)	f_e	$\frac{(C_e - e_{av})^2}{(1+e_{av})} \cdot \frac{(1+e_{max})}{(C_e - e_{max})^2}$	$\begin{cases} 1, & e_{av} \geq e_{max} \\ 0, & e_{av} < e_{max} - \frac{1}{C_e} \\ 1 - C_e(e_{max} - e_{av}), & \text{otherwise} \end{cases}$	C_e, e_{max}	e_{av}
(7)	f_p	$\exp\left(-C_p \cdot \left(\frac{p'_{av}}{101.3\ [kPa]} - 1\right)\right)$	*no modification*	C_p	p'_{av}
(8)	f_Y	$\exp(C_Y \cdot \bar{Y}_{av})$ $\bar{Y}_{av} = \frac{\frac{I_1 I_2}{I_3} - 9}{8 \tan^2 \phi'_{cs}}$	$\exp\left(C_Y \cdot \frac{J_{av}/p'_{av}}{g(\phi'_{mag}, \theta_{av})}\right)$ $g(\phi'_{mag}, \theta_{av})$ is the available strength defined by the Mohr-Coulomb failure criterion expressed in stress ratio terms.	C_Y, ϕ'_{mag}	$p'_{av}, J_{av}, \theta_{av}$
(9)	$[D^{ela}_{HCA}]$	Isotropic tangent elastic stiffness matrix, defined by the HCA bulk and shear moduli: $K^{ela}_{HCA} = K_{ref,HCA} \frac{(1.63 - e_{av})^2}{1 + e_{av}} \left(\frac{p'_{av}}{101.3}\right)^{0.5}$ $G^{ela}_{HCA} = \frac{3K^{ela}_{HCA}(1 - 2\nu_{HCA})}{2(1 + \nu_{HCA})}$	*no modification*	$K_{ref,HCA}, \nu_{HCA}$	e_{av}, p'_{av}

p', J, θ are conventional soil mechanics stress invariants and e and e_{max} are the current and maximum void ratios,

ϕ'_{cs} is the low-cycle model critical state strength, ϕ'_{dir} the angle of shearing resistance defining the direction of strain accumulation using the normal to the Modified Cam Clay surface and ϕ'_{mag} is a reference angle of shearing resistance to assess the contribution of current stress ratio on strain accumulation,

$g(\phi', \theta)$ describes the Mohr-Coulomb failure criterion in the π-plane: $\frac{\sin(\phi')}{\cos(\theta) + \sin(\theta)\frac{\sin(\phi')}{\sqrt{3}}}$,

C_{ampl}, C_e, C_p, C_Y are material parameters controlling the cyclic strain amplitude, void ratio, mean effective stress and stress ratio contributions to the magnitude of strain accumulation, C_{N1}, C_{N2} are material parameters controlling the rate of accumulation with cycles,

g_{cyc} and $g_{cyc}(N_0)$ are values of the current cyclic history variable and at the start of current cyclic package at $N = N_0$,

Subscript $_{av}$ denotes the average trend value during high-cycle or accumulation phases,

ε^{ampl} and ε^{lim} are cyclic strain amplitude and reference limit strain amplitude respectively,

Note that definitions of superseded variables (Niemunis et al., 2005) are omitted for brevity.

135

The effects of void ratio f_e, mean effective stress f_p, normalised stress ratio f_Y and cyclic history g_{cyc} on accumulated strain are treated by Niemunis et al. (2005) as:

$$\{\Delta\varepsilon^{acc}\} = \Delta N \cdot \left\{\frac{\partial \varepsilon^{acc}}{\partial N}\right\} = \Delta N \cdot \{\vec{m}\} \cdot \frac{\partial g_{cyc}}{\partial N} \cdot f_e f_p f_Y \tag{10}$$

where $\{\vec{m}\}$ is a unit direction vector and ΔN is an increment in number of cycles. While the pressure dependent factor f_p remains unchanged, the void ratio and stress ratio dependencies f_e and f_Y have been simplified to avoid discontinuities in the original formulation. Accumulation direction $\{\vec{m}\}$ is also decoupled from f_Y to better fit Dunkirk sand, extending the HCA framework to allow for its application in a wider range of sands through the calibration procedure described for Dunkirk sand. From the accumulation laws summarised by Chong & Santamarina (2016), Liu (2018) showed that Dunkirk sand's drained cyclic triaxial tests' strain accumulation trends were better fitted using power than log-linear curves. Details of all numerical modifications and derivation of a new cyclic history variable $g_{cyc} = f_{ampl} \cdot f_N$ in equation (5) are found in Tantivangphaisal et al. (2025). The authors employed the Wichtmann et al. (2013) elastic stiffness matrix, relating per-cycle strain accumulation to stress relaxation, as summarised with other HCA equations in Table 2.

2.3 Numerical implementation in a FE software

Robust use of low-cycle elasto-plastic constitutive models with the HCA framework requires consideration of how underlying state variables evolve during accumulation. The adaptive strain approach (Staubach et al., 2022b) has been applied to develop a strain space state variable evolution rule during high-cycle accumulation. Tantivangphaisal et al. (2024, 2025) give further details of the constitutive model's numerical integration, software-specific implementation strategy and verification against independent work.

3 Low-cycle model parameters for Dunkirk sand

Low-cycle model calibration relies on site-specific piezo-cone and seismic cone penetration (SCPT) profiling, as well as drained and undrained triaxial compression tests. The profiles established for Dunkirk (Chow, 1997; Kuwano, 1999; Aghakouchak, 2015; Liu, 2018; Zdravkovic et al., 2020) led to the calibrated model parameters in Table 3. At the same site and for the same set of piles, Zdravkovic et al. (2020) summarised the

relative density profile interpreted from cone penetration tests utilising approaches by Baldi et al. (1986) and Kulhawy and Mayne (1990). The in-situ void ratios were then computed using limits of $e_{max} = 0.91$ and $e_{min} = 0.54$ determined in the laboratory (Liu, 2018).

3.1 Elastic stiffness at very small strains

The SCPT G_{max} values, normalised by the Hardin & Richart (1963) void ratio relationship, are plotted on logarithmic axes against in-situ mean effective stress in Figure 2, assuming $K_0 = 0.4$ after the site-specific assessment in Chow (1997) and bulk densities of 17.1 $[kN/m^3]$ and 19.9 $[kN/m^3]$ above and below a water table depth of 5.4 m. A linear best fit gave the G_{ref} and m_G values defined in equation (A.1) as shown in Figure 2. The initial shear modulus with depth assessed from SCPT shear wave velocity profiles, is well reproduced and intrinsically linked in the calibration process with the assumed initial lateral stresses. Poisson's ratio ν was determined by Liu (2018) from high-resolution triaxial compression tests on medium dense and dense Dunkirk sand.

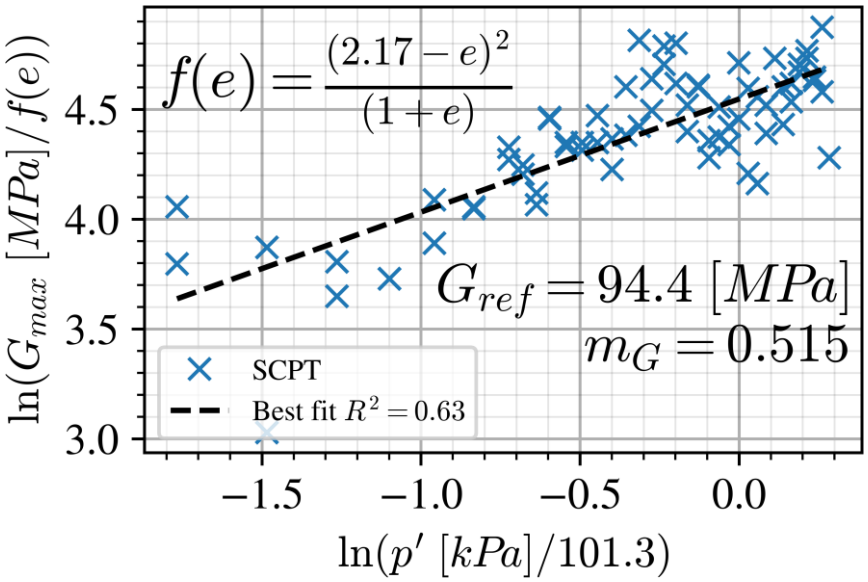


Figure 2 Least square fit for reference elastic shear stiffness G_{ref} and pressure-dependent exponent m_G, assuming in-situ $p'_0 = (1 + 2K_0) \cdot \sigma'_v/3$ with $K_0 = 0.4$.

3.2 Critical state and peak strength envelope

The critical state line in equation (A.2) employs the parameters interpreted for earlier PISA monotonic analyses (Taborda et al., 2020) from Dunkirk sand tests by Aghakouchak (2015). The shear strength is assumed linearly dependent on state-parameter ψ with

slope k. The slope and intercept M_{cs} in equation (A.3) were fitted from the five drained laboratory tests plotted in Figure 3 (Taborda et al., 2020).

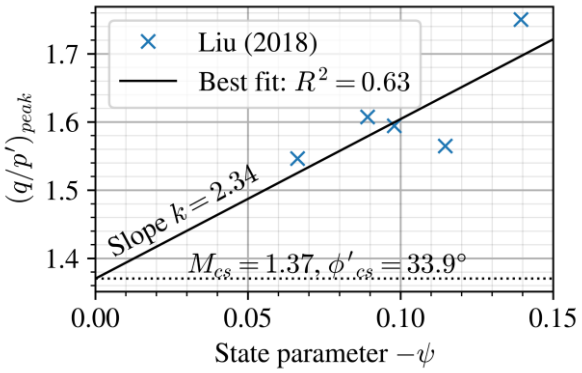


Figure 3 Determining low-cycle model parameters for critical state and peak strength.

3.3 Plastic dilatancy at larger strains

The model's non-associated plastic potential is engaged after achieving peak strength. In drained triaxial tests, the plastic dilation rate D_p is approximately equal to the ratio of total volumetric and deviatoric strain rates $D = \Delta\varepsilon_{vol}^{tot}/\Delta\varepsilon_{d}^{tot}$. Parameter l in equation (A.4) is obtained from linear regression of D values against state parameter from drained triaxial tests (see Figure 4).

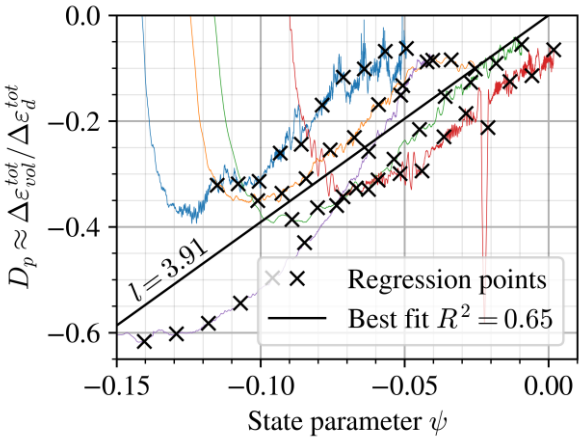


Figure 4 Dilation against state parameter from drained triaxial tests.

As discussed in Loukidis & Salgado (2009), D_p values interpreted from undrained laboratory tests are highly sensitive to the assumed K^{ela}. With the model's open yield surface and strain-dependent tangent elastic moduli, D_p predicted under undrained or constant volume shearing is reflected by the value of $K_{tan}^{ela} = K_{min} = R_{min} \cdot K_{max}$. An appropriate R_{min} for this model is determined first by calculating undrained plastic

dilation $D_p^* = \frac{-\Delta p'}{K_{max}} \frac{1}{\Delta \varepsilon_d^{tot}}$ from laboratory data using the maximum, non-degraded elastic stiffness K_{max}.

A large discrepancy between D_p and D_p^* owing to the use of K_{max} to calculate D_p^* is seen in Figure 5.

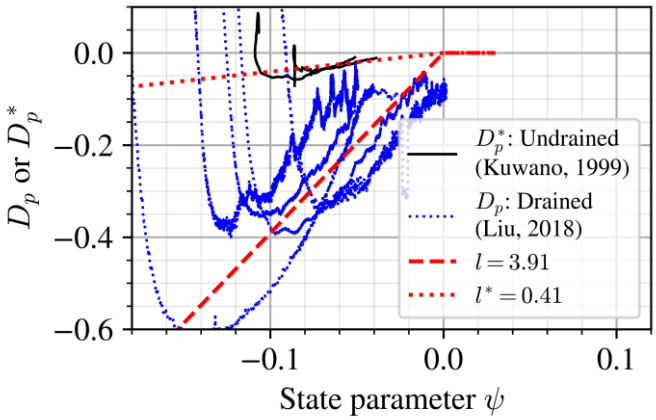


Figure 5 Plastic dilation analysed from drained and undrained Dunkirk sand triaxial compression tests (Kuwano, 1999; Liu, 2018) and respective trends.

By adopting $R_{min} = 0.104$ equal to the ratio of the drained ($l = 3.91$) and undrained ($l^* = 0.41$) slopes, the model can predict the same plastic dilation trends under drained or undrained conditions:

$$\frac{l^*}{l} = \frac{D_p^*}{D_p} = \frac{-\frac{\Delta p'}{K_{max}} \frac{1}{\Delta \varepsilon_d^{tot}}}{\frac{-\Delta p'}{K_{min}} \frac{1}{\Delta \varepsilon_d^{tot}}} = \frac{K_{min}}{K_{max}} = R_{min} \tag{11}$$

3.4 Shear stiffness degradation

The low-cycle model's modified hyperbolic degradation curve for the tangent elastic shear modulus G_{tan} is controlled by parameters a, b and R_{min} in equation (A.5). The role of each is described in Taborda & Zdravkovic (2012) and Taborda et al. (2016).

Applying the calibrated R_{min}, a non-linear regression for parameters a and b is carried out against tangent stiffness trends taken from locally instrumented triaxial tests (Liu, 2018; Liu et al., 2022b), normalised by the corresponding value of G_{max} determined using equation (A.1) (see Figure 6).

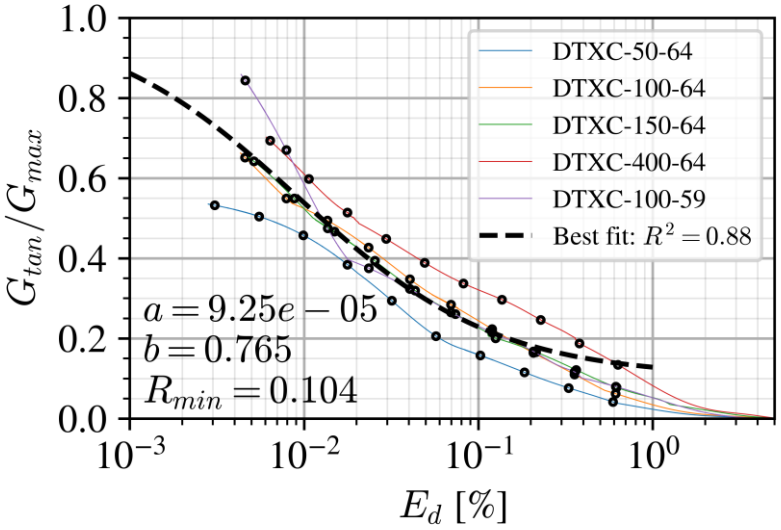


Figure 6 Best fit of shear modulus degradation curve parameters a, b up to $E_d =$ 1% from locally instrumented drained triaxial compression tests.

3.5 Monotonic response

Single element simulations made with the calibrated parameters listed in Table 3 are compared with triaxial experimental data in Figure 7, showing generally good fits to the experimental non-linear stress-strain responses and shear-volumetric coupling from small strains to critical states, under a range of density and pressure conditions in the range of values anticipated for the engineering problem at hand.

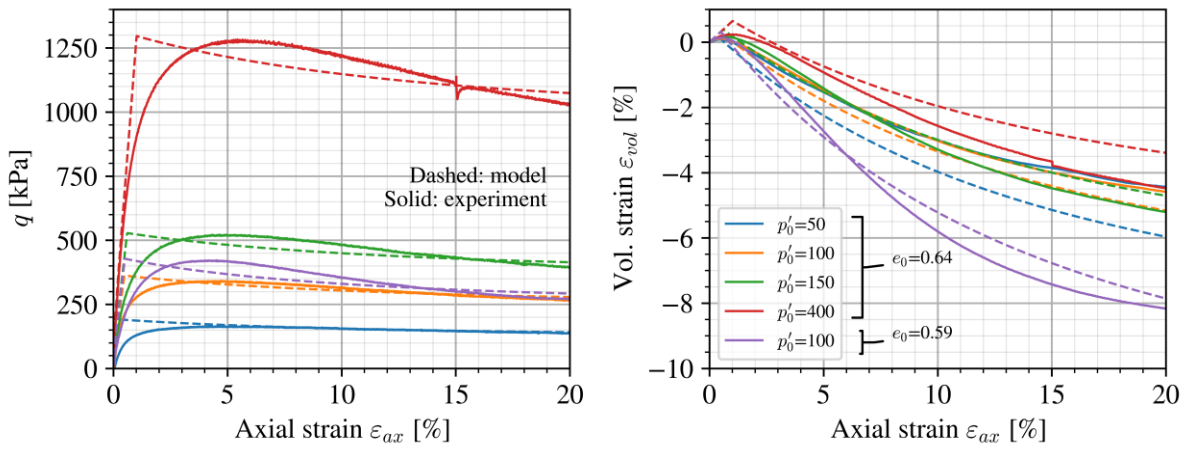


Figure 7 Calibrated low-cycle model response in drained triaxial tests.

Table 3 Summary of low-cycle model parameters calibrated for Dunkirk Sand.

Parameter	G_{ref} (MPa)	m_G	ν	a (%)	b	R_{min}	$e_{cs,ref}$	λ	ξ	ϕ'_{cs} (°)	k	l
Value	94.4	0.515	0.180	$9.25 \cdot 10^{-3}$	0.765	0.104	0.910	0.135	0.179	33.9	2.34	3.91

4 High-cycle parameters for Dunkirk sand

4.1 Calibration rationale

The HCA framework has been calibrated for Dunkirk sand against triaxial tests that imposed regular stress cycles. The rates of change in averaged conventional soil mechanics triaxial stress and strain quantities over sets of N cycles, as given in Equation (12) are illustrated in Figure 8a.

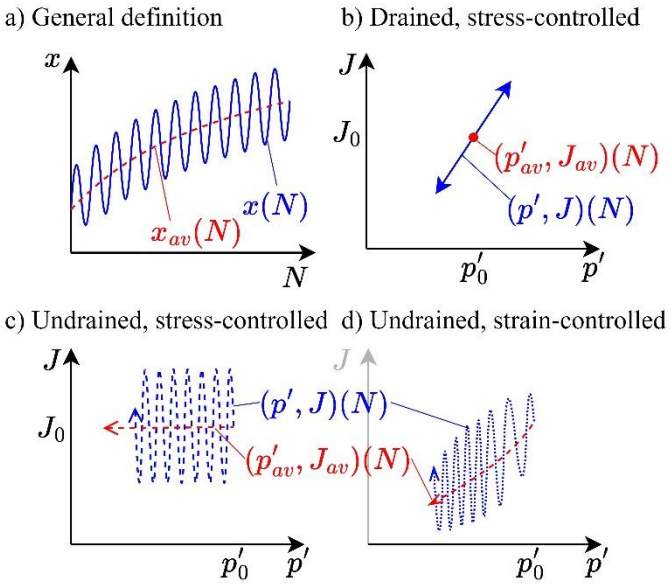


Figure 8a) General definition of quantities averaged over N cycles; b, c, d) schematic of possible cyclic triaxial stress paths.

$$\begin{Bmatrix} \frac{\partial p'_{av}}{\partial N} \\ \frac{\partial J_{av}}{\partial N} \end{Bmatrix} = \begin{bmatrix} K_{tan}^{HCA,ela} & 0 \\ 0 & G_{tan}^{HCA,ela} \end{bmatrix} \left(\begin{Bmatrix} \frac{\partial \varepsilon_{vol,av}^{tot}}{\partial N} \\ \frac{\partial E_{d,av}^{tot}}{\partial N} \end{Bmatrix} - \begin{Bmatrix} \frac{\partial \varepsilon_{vol,av}^{acc}}{\partial N} \\ \frac{\partial E_{d,av}^{acc}}{\partial N} \end{Bmatrix} - \begin{Bmatrix} \frac{\partial \varepsilon_{vol}^{pl}}{\partial N} \\ \frac{\partial E_{d}^{pl}}{\partial N} \end{Bmatrix} \right) \quad (12)$$

In equation (12), $K_{tan}^{HCA,ela}$ and $G_{tan}^{HCA,ela}$ are respectively the tangent elastic HCA bulk and shear moduli relating the rate of change in average stresses with rate of change in average elastic strains during long-term cycling. Wichtmann et al. (2010b, 2013) confirmed these stiffness values depend on pressure and density, as under monotonic loading.

Following classical plastic shakedown and ratcheting theories, the cyclic stress-strain response of sands can be generalised into four stable or metastable regimes (Collins & Boulbibane, 2000): 1) fully recoverable elastic response, 2) elastic shakedown, with

closed hysteretic stress-strain loops, 3) plastic shakedown and 4) plastic ratcheting until some terminal state (Narsilio & Santamarina, 2008). Schematics of stress paths seen in cyclic triaxial tests during the metastable plastic shakedown and plastic ratcheting regimes are shown in Figure 8b and 8c for stress-controlled tests and Figure 8d for strain-controlled tests.

An upper bound cyclic strain amplitude of 0.1% (Niemunis et al., 2005) was originally proposed for the HCA framework to capture the behaviour observed in drained laboratory tests which fall within these qualitatively described regimes. Liu (2018) noticed that stress-controlled drained tests carried out at large initial stress ratios ($q_0/p'_0 = 1.2$) with applied cyclic stress ratios ($CSR = \Delta q/(2p'_0)$) of 0.4 to 0.5 resulted in 'incremental collapse' after a certain number of cycles. This was defined as uncontrolled plastic flow and failure where strains over the last cycle greatly exceeds the prior averaged trend.

Incremental collapse within any single cycle cannot be accounted for in the HCA framework. However, for general stress paths, the plastic strain term produced by elasto-plasticity provides a numerical mechanism for collapse. To ensure consistency this occurs when the stress state coincides with the low-cycle's yield surface.

The known boundary conditions of each test type can be substituted into Equation (12) allowing for a stepwise calibration of each HCA constituent part as illustrated in Table 4.

Table 4 Cyclic element test type and corresponding HCA constituent part.

Type of cyclic triaxial test		**Boundary conditions**	**Enables calibration of**
Load control	**Drainage conditions**		
Stress cycles	Drained	$\frac{\partial p'_{av}}{\partial N} = 0, \frac{\partial J_{av}}{\partial N} = 0$	$\{\vec{m}\}, \frac{\partial g_{cyc}}{\partial N}, f_e, f_p, f_Y$
	Undrained	$\frac{\partial \varepsilon^{tot}_{vol,av}}{\partial N} = 0, \frac{\partial J_{av}}{\partial N} = 0$	$K^{HCA,ela}_{tan}$
Strain cycles		$\frac{\partial \varepsilon^{tot}_{vol,av}}{\partial N} = 0, \frac{\partial E^{tot}_{d,av}}{\partial N} = 0$	$\nu^{HCA} = \frac{3K^{HCA} - 2G^{HCA}}{2(3K^{HCA} + G^{HCA})}$

The simplification of loading conditions into packages of regular cycles that vary about an average static load as required in the HCA framework, requires the definition of when the first regular cycle begins, i.e. when 'accumulation' first starts. This was defined to

begin after any 'irregular loading' by both the original formulation (Niemunis et al., 2005) and subsequent developments (Wichtmann, 2005, 2016; Staubach, 2022).

A schematic of the stress-strain history of an arbitrary point in the ground is illustrated in Figure 9 with descriptions of each state. Conceptual consistency is maintained from calibration using monotonic and cyclic element tests, through to the low-cycle modelling and the finite element analyses of the field problem.

This is achieved in three ways:

1. The stress and strain states in the element test immediately before cyclic load application should correspond to those at the end of stage [C].
2. Stage [D] in Figure 9 is considered an 'irregular' cycle whose strain accumulation or stress relaxation is accounted for by the low-cycle model, regardless of whether stage [C] modified the stress and strain states within the ground. This brings in line the treatment of single element tests cycled about the isotropic stress axis with those about an anisotropic or pre-loaded average stress state.
3. The selected and calibrated low-cycle model is used to calculate strain amplitude ε^{ampl} and cyclic history state variable g_{cyc} during HCA single element calibration. In contrast with Wichtmann et al. (2010a), who fed the strain amplitudes from laboratory tests directly into the calibration process, this approach ensures consistency between the low-cycle model and HCA framework from its calibration through to the boundary value problem analyses.

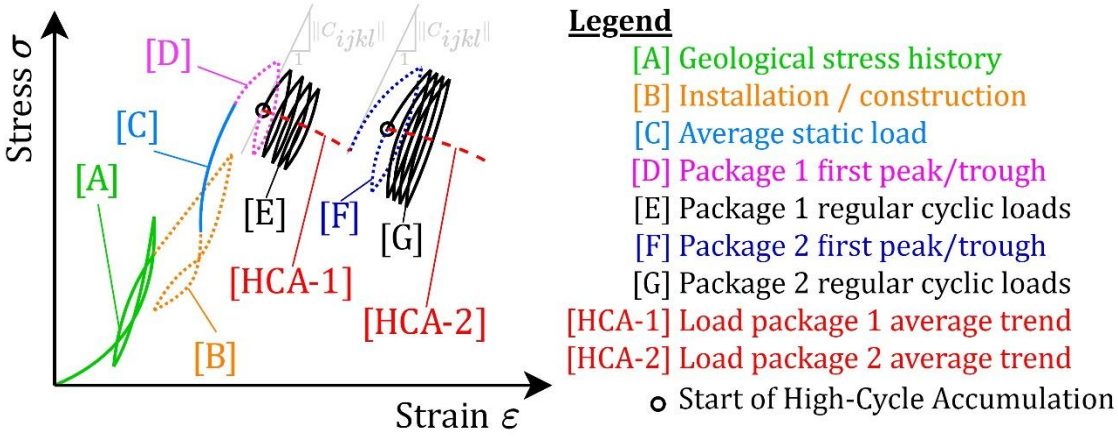


Figure 9 Schematic of HCA definitions on a general stress-strain path.

Between different cyclic load packages, the HCA state variable g_{cyc} governs how previous cycles of different magnitudes affect future accumulation trends. Experiments

(Wichtmann et al., 2010b; Lopez-Querol & Coop, 2012; Knittel et al., 2023) indicate that some 'erasure' or 'reset' of cyclic history occur if the magnitude of subsequent loading exceeds that of previous cycles. Wichtmann & Triantafyllidis (2017) and Knittel et al. (2023) have shown that this reset could be correlated with the ratio between the strains caused by subsequent loading and previous cyclic strains. A reset of g_{cyc} to zero is employed between accumulation phases in the reported HCA analyses when loads applied during intermediate low-cycle phases exceed those in previous cycles. This avoids the significant underestimation of strain accumulation under increasing load cycles at increasing shear stress levels identified by Wichtmann & Knittel (2020).

4.2 Calibration procedure

Dunkirk sand HCA parameters were derived from effective stress paths, strain accumulation and amplitude data from 17 stress-control drained cyclic triaxial tests and 5 stress-control undrained cyclic triaxial tests by Liu (2018). Drained test conditions covered a range of initial void ratios $e_0 \in [0.632,\ 0.716]$, initial mean effective stresses $p'_0 \in [100,\ 400]$ kPa, initial stress ratios $\eta_{av} \in [0,\ 1.2]$, cyclic stress amplitudes $CSR \in [0.1,\ 0.5]$, defined as $\Delta q/2p'_0$ with $\Delta q = q_{max} - q_{min}$. Cycle numbers exceeded 10,000 for all tests but one (to $N = 6287$). Undrained tests were carried out at $p'_0 = 100$ kPa, $e_0 \in [0.637, 0.660]$ and $CSR \in [0.1,\ 0.3]$.

All presented tests were normally consolidated and carried out on water-pluviated, fully saturated 38mm diameter, 2:1 height-diameter samples, employing enlarged lubricated platens and high-resolution local strain instruments. Shearing cycles were applied at 0.00833 Hz. These tests were designed to assess the strain accumulation characteristics of Dunkirk sand under regular loading cycles prior to reaching the material's failure envelope.

4.2.1 Direction of strain accumulation

The ratio of volumetric to deviatoric strain accumulation is based on the vector normal to the Modified Cam Clay (MCC) surface fitted through the average stress state invariants $p'_{av}, J_{av}, \theta_{av}$ with its size defined by ϕ'_{dir}. As the average stress states of all DcycTX tests lie on the triaxial compression side, the ratio of the deviatoric to volumetric plastic flow direction is evaluated at $\theta_{av} = -30°$.

The directional derivatives of the MCC surface are:

$$\frac{\partial}{\partial p'_{av}} = \frac{1}{{p'_{av}}^2} - \frac{2J_{av}^2}{{p'_{av}}^3 g^2(\theta)}; \quad \frac{\partial}{\partial J_{av}} = \frac{2J_{av}}{\left(p'_{av} g(\theta)\right)^2} \tag{13}$$

And the ratio $(\frac{\partial}{\partial p'_{av}})/(\frac{\partial}{\partial J_{av}})$ is denoted as ω^{acc}:

$$\omega^{acc} = \frac{g^2(\phi'_{dir}, \theta_{av} = -30°) - \left(\frac{J_{av}}{p'_{av}}\right)^2}{\frac{2J_{av}}{p'_{av}}} = \frac{\left(\frac{2\sqrt{3}\sin\phi'_{dir}}{3 - \sin\phi'_{dir}}\right)^2 - \left(\frac{J_{av}}{p'_{av}}\right)^2}{\frac{2J_{av}}{p'_{av}}} \tag{14}$$

An average direction $\bar{\omega}^{acc}$ is calculated from laboratory strain data using anisotropically consolidated tests by:

$$\bar{\omega}^{acc} = \frac{1}{N_{total}} \int \left(\frac{\Delta\varepsilon_{vol}^{acc}}{\Delta E_d^{acc}}\right) dN \tag{15}$$

The evolution of ω^{acc} is plotted against number of cycles in Figure 10a and a best fit $\phi'_{dir} = 26.8°$ in $\bar{\omega}^{acc} - (J_{av}/p'_{av})$ space is shown in Figure 10b. The original formulation adopting the critical state angle of shearing resistance for ϕ'_{dir} is shown in red and lies well above laboratory data.

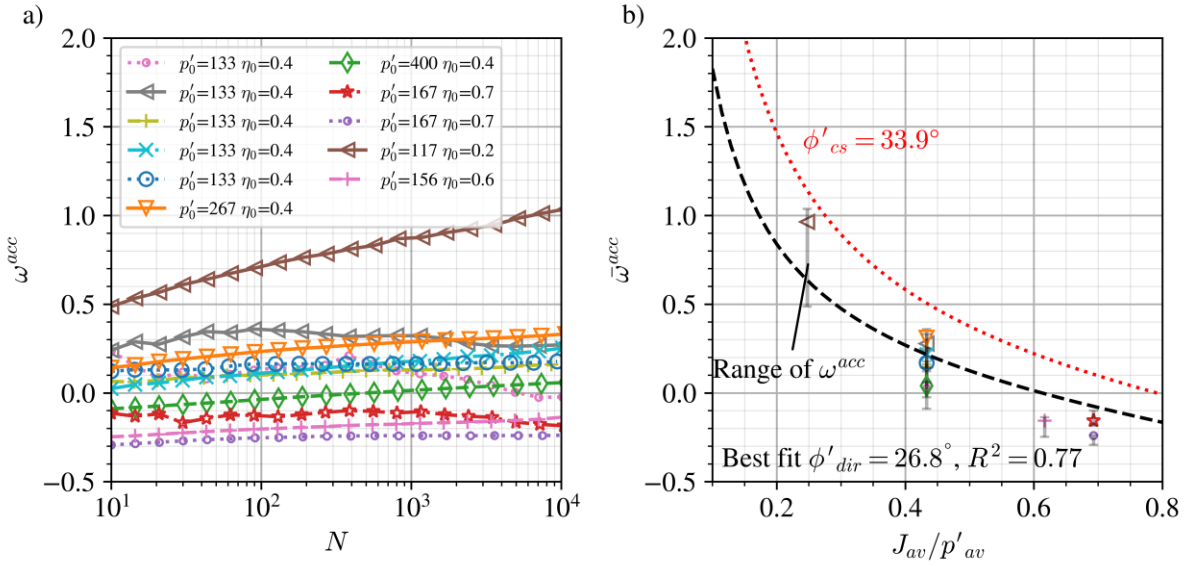


Figure 10 Direction of strain accumulation from drained cyclic tests in Dunkirk sand showing a) response with number of cycles and b) averaged to fit ϕ'_{dir}.

4.2.2 Magnitude of strain accumulation

The current calibration uses a genetic algorithm (GA) (Holland, 1992) implemented for general geotechnical optimisation problems (Ruiz López, 2024). A bespoke modified-Euler integration driver for equation (10) was used to evaluate the fitness function. From

the laboratory data, the scalar value of accumulated strain is calculated from end-of-cycle local readings of axial and radial strains as $\|\varepsilon^{acc}\| = \sqrt{\varepsilon_{ax}^{acc\,2} + 2\varepsilon_{rad}^{acc\,2}}$. The calibrated low-cycle model is used in the driver to calculate and update the underlying ε^{ampl} state variable given current e_{av}, p'_{av} states during integration. This makes the calibration process of both low- and high-cycle parts of the constitutive consistent with how the final boundary value problem is computed with continuous re-engagement of the low-cycle model.

Parameters governing magnitude of strain accumulation, $C_{ampl}, C_{N1}, C_{N2}, C_e, C_p, C_Y$, are optimised by maximising the GA fitness computed as the reciprocal of the sum squared error between model response and laboratory data at 20 evenly spaced points in log(N) space. All tests carried equal weight. An additional sensitivity check using 50 data points per test and wider parameter bounds resulted in a negligible change in the optimised parameter set. Figure 11 compares the calibrated model response with experimental strain accumulation results. Considering the wide range of initial and loading conditions applied in the testing (six mean effective stress levels, two densities and four cyclic stress ratios), the laboratory data is generally well-reproduced. Robustness in the optimisation is ensured by taking modal values from the best 1000 candidates rather than a single best individual.

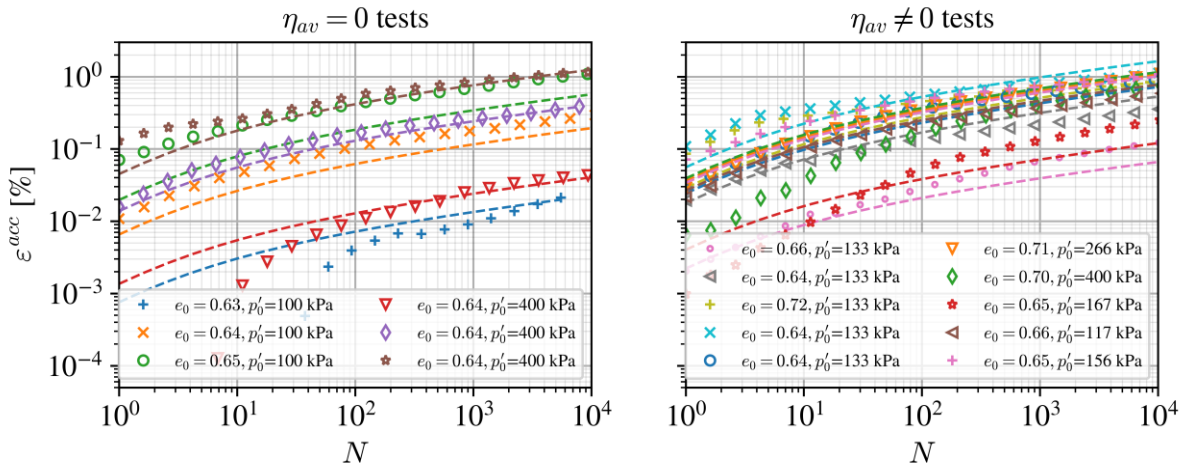


Figure 11 Drained single element experimental strain accumulation compared against model prediction.

4.2.3 Stress relaxation-strain accumulation coupling

The magnitude of $K_{ref,HCA}$ governs coupling between predicted strain accumulation and stress relaxation. Stress-relaxation may be significant where the soil mass shears with restricted volume change even when considering fully drained cyclic monopile boundary value problems. $K_{ref,HCA}$ was calibrated from the pore pressure response from undrained cyclic tests, using the integration driver and genetic algorithm optimisation described above, leading to the outcomes shown in Figure 12 for five tests at $e_0 = 0.63$ and $p'_0 = 100$ kPa. The adopted modelling approach captures the observed trends adequately, although there is some overprediction of pore water pressure build up under lower CSR and underprediction of rates at higher CSR. This is likely because the natural Dunkirk marine sand does not fully adhere to the same empirical forms of void-ratio- and stress-dependent pore water accumulation as that derived from extensive tests of a reconstituted laboratory sand with a prescribed grading curve (Wichtmann et al., 2010a, 2013). Further tests on a range of natural soil types offer the potential to improve the HCA framework's pore pressure accumulation prediction, particularly for problems such as liquefaction or for use with low-permeability soils.

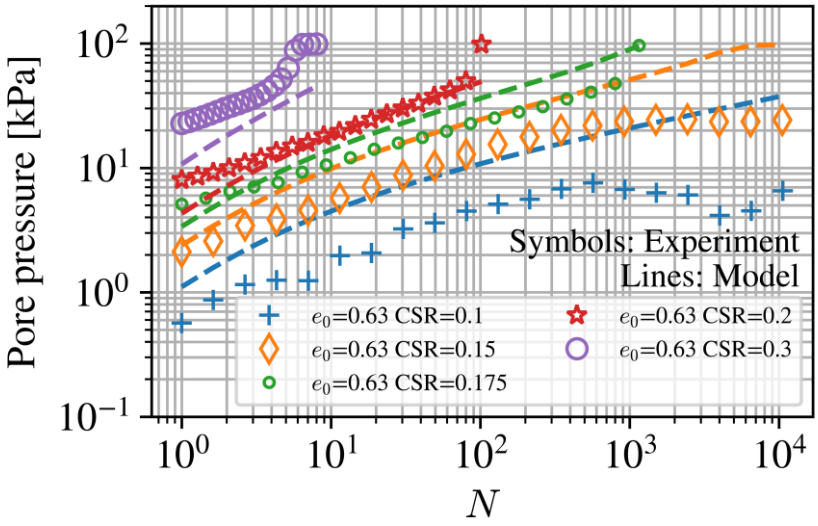


Figure 12 Calibrated model compared against undrained pore pressure per cycle.

As strain-controlled undrained cyclic triaxial tests were not conducted on Dunkirk sand samples, $\nu_{HCA} = 0.32$ was taken as found for Karlsruhe fine sand by Wichtmann et al. (2013). Checks showed that the field monopile analyses were insensitive to this choice.

The final set of HCA parameters for Dunkirk sand, which are fully compatible with the low-cycle constitutive model, is listed in Table 5.

Table 5 Summary of HCA framework material parameters for Dunkirk sand.

ϕ'_{dir} (°)	C_{ampl}	ε^{lim} (%ε)	C_{N1}	C_{N2}	C_e	e_{min}	e_{max}	C_p	C_Y	ϕ'_{mag} (°)	$K_{ref,HCA}$ (MPa)	ν_{HCA}
26.8	1.52	0.1	$2.29 \cdot 10^{-4}$	0.167	0.168	0.540	0.910	0.222	1.49	33.9	91.2	0.320

5 Field test details

Cyclic (Byrne et al., 2020) and monotonic lateral pile load tests (McAdam et al., 2020) were carried out on 0.76m and 2m diameter open-steel piles driven at Dunkirk under the PISA project. The main long-term quasi-static cyclic load testing was carried out on the 0.76m pile DM2, with sequentially increasing one-way lateral load cycles to 10, 20, 40, and 80 kN applied at 0.1 Hz frequency. These maximum load levels correspond to approximately 5, 10, 20 and 40% of the ultimate limit load, defined by the monotonic capacity at a pile head displacement of 10% pile diameter. The loading extended to 5100, 3300, 8100 and 11110 cycles respectively at each level.

5.1 Problem geometry

The present high-cycle study focused on pile DM2, whose general arrangement is shown in Figure 13. The 14mm thick (L/D = 5.2) steel pile was modelled using 6-noded shell elements with an isotropic linear elastic material model with Young's modulus $E = 200$ MPa and Poisson's ratio $\nu = 0.3$. Staubach et al. (2024) recently discussed the need to model installation effects for laboratory scale model tests in dry soils with very low confining stresses. Considering the current boundary value problem is mainly governed by the behaviour of a large volume of surrounding soil, although localised installation effects are present, various studies show piles modelled as wished-in-place or driven using a variety of methods in medium dense to dense sands show broadly comparable lateral load-displacement behaviour and ultimate capacities. The current modelling thus follows Taborda et al. (2020) and the pile was 'wished-in-place'. The pile shaft to soil interface was modelled using 12-noded zero-thickness interface elements with a Coulomb failure criterion. The interface strength was adopted as the same ϕ'_{cs} from the surrounding soil following interface shearing tests by Liu (2018). Parameters for the normal stress (σ'_n) dependent elastic interface were selected based on the stiffness properties of the surrounding soil to prevent numerical difficulties due to an over-stiff

interface but stiff enough to have negligible effect on the result. The corresponding shear stiffness $k_s = 1.59 \cdot 10^6 \cdot (\sigma_n'/101.3)^{0.423}\ kN/m^3$ and normal stiffness $k_n = k_s \cdot (2(1 - \nu_{int})/(1 - 2\nu_{int}))$ where $\nu_{int} = 0.45$ (Bentley Systems, 2024).

Full drainage was assumed. The soil layers were discretised to capture the field distributions of void ratio, bulk unit weight and static pore water pressures (Taborda et al., 2020). A total of 30,243 10-noded quadratic tetrahedral elements each with 4 integration points were used to discretise the soil domain. Element edge immediately adjacent to the pile shaft were kept at, or less than, no larger than 0.05m on each edge to ensure calculation accuracy in zones of high stress gradients. This element size was selected by evaluating the equivalent displacement (p-y) and rotational (m-θ) springs as derived from interface nodal forces (Burd et al., 2020b) computed in lateral monotonic analyses that extended to a pile head displacement of 10% pile diameter. Checks confirmed that the results obtained were insensitive to any further refinement of the mesh. Extensive mesh sensitivity studies were performed to ensure the discretisation was adequate, with further refinement showing no measurable impact on the obtained response. Similarly, the chosen domain dimensions (Figure 13) were found sufficiently large to avoid boundary effects. A single set of parameters calibrated using only site investigation and laboratory test data is used for all analyses for both low- and high-cycle behaviour without any recalibration to match field-scale test pile measurements.

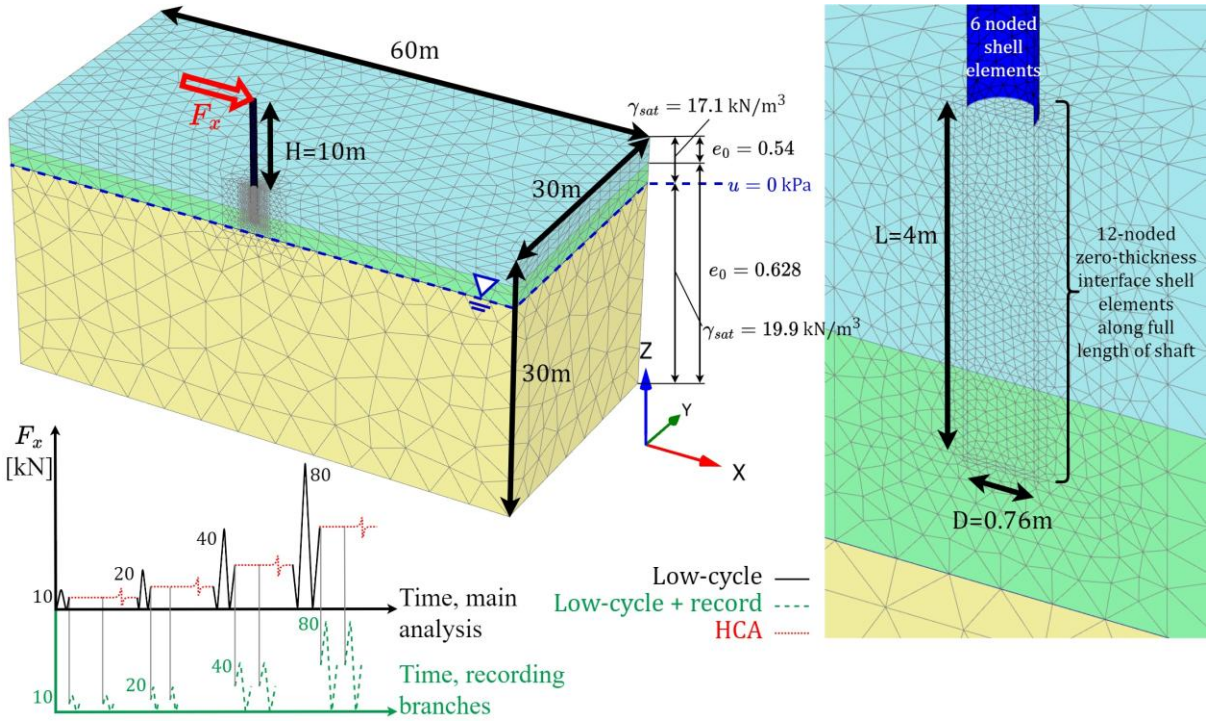


Figure 13 Details of the medium sized 0.76m diameter pile FE model.

6 Predictions and field measurements

6.1 Monotonic and single-cycle response of the low-cycle model

The low-cycle model's ability to match field monotonic loading behaviour was tested against pile head measurements made with both 0.76m (DM4, equivalent dimensions to the cyclic DM2 pile) and 2m (DL2) diameter piles. Applying the area difference accuracy metric $\eta_{accuracy}$ to $D/10$ (Burd et al., 2020b) confirms that the low-cycle model predictions shown in Figure 14 replicate the piles' field monotonic load-unload behaviour ($\eta_{accuracy} = 85\%$ and 90%, respectively and similar to the response reported by Taborda et al. (2020)).

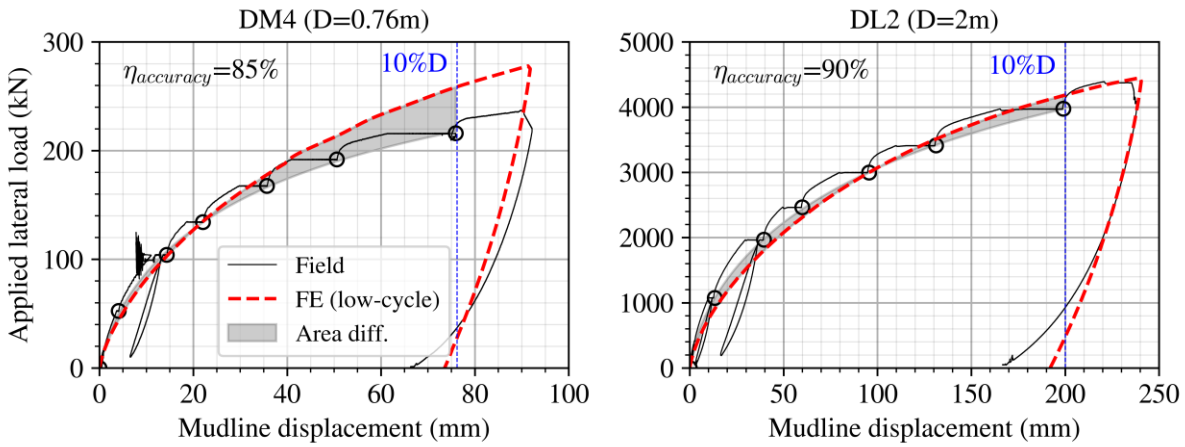


Figure 14 Load-unload pile response to ultimate capacity – calibrated low-cycle model compared against field data.

The single-cycle pile head moment-rotation response is also well captured by the low-cycle model, as shown in Figure 15, where different scales are used for the various loading amplitudes for clarity. The predicted response at the lowest (10kN) load cycle appears to deviate farthest from the measured response. However, field rotations (in the order of 0.01°), derived from relative displacements measured at different heights (Burd et al., 2020a), should be treated with caution given the difficulty of measuring such small values accurately. The 20, 40 and 80kN cyclic moment-rotation predictions match the field measurements well.

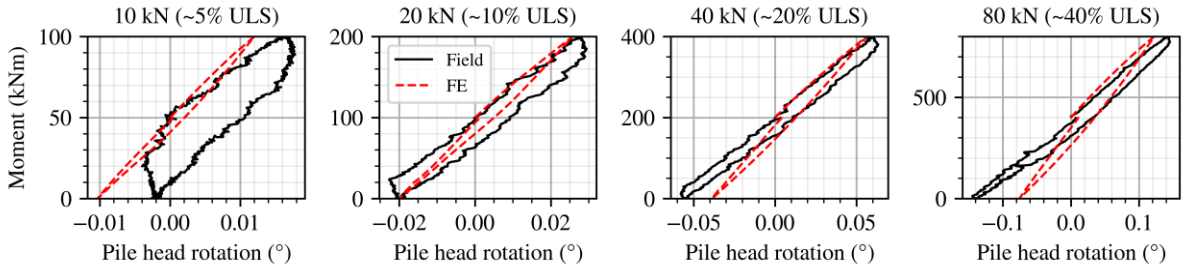


Figure 15 Moment-rotation response over single regular cycles compared with field data.

6.2 High-cycle comparison

As detailed in Appendix table B-1, the field lateral loading sequence applied to pile DM2 was followed faithfully in the high-cycle FE analyses. The 5100 (10kN), 3300 (20kN), 8100 (40kN) and 11110 (80kN) cyclic packages were applied sequentially in a single analysis, re-zeroing the history variable g_{cyc} at the start of each package. The resulting pile head level displacements and rotations are presented in Figure 16. Several HCA

update cycles (shown as vertical dashed lines) were applied per package, with sensitivity checks confirming that more frequent updating had no influence. Although the modelling over-predicted the displacements and rotations observed for 20 kN cycling, the three other predictions plot closer to the field trends.

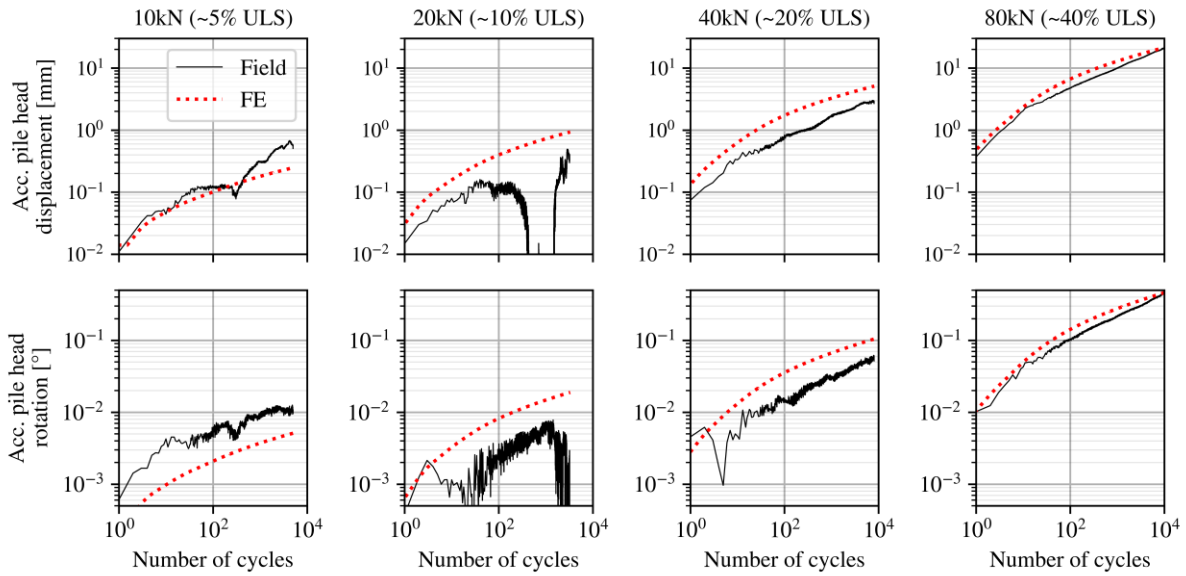


Figure 16 Pile response compared with measured field data at pile head at four different load levels, referenced to zero at the start of each load package.

The simulated rotation-depth trends also showed a good match with the field data; measurements made at the front and back of the pile are shown as dual readings for the 80 kN cyclic load package depicted in Figure 17, while the FE model rotations were calculated using front and back nodal vertical displacements.

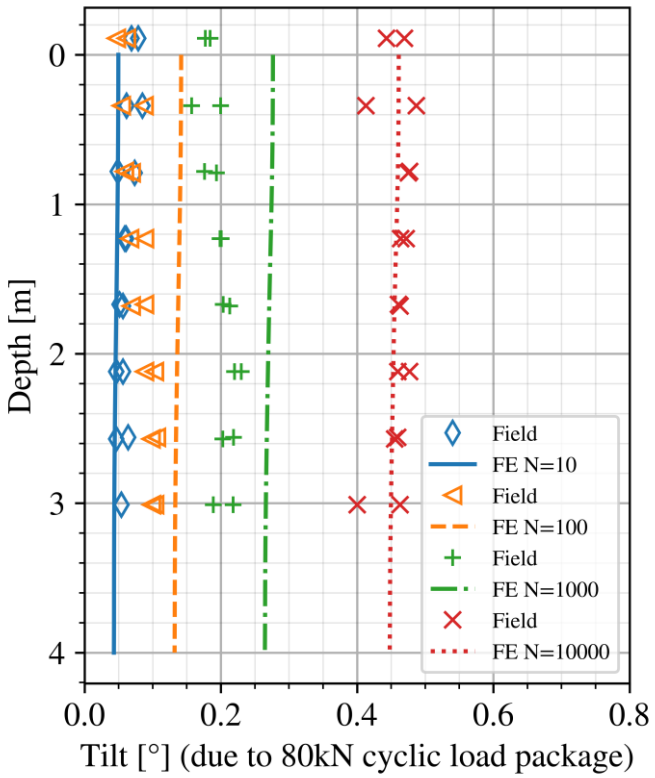


Figure 17 Comparison of computed pile rotation with field inclinometer readings.

A major benefit of modelling the 3D soil domain and pile-soil interaction using finite elements is the possibility to explore and attribute associated physical mechanisms to globally observed phenomena. In Figure 18, the application of "pre-loading" due to the 10, 20 and 40kN one-way load packages is seen to increase the initial stiffness of the pile relative to the reference monotonic curve. This feature was captured by the coupled low-cycle and modified HCA modelling over the pile re-loading stages imposed after each load package.

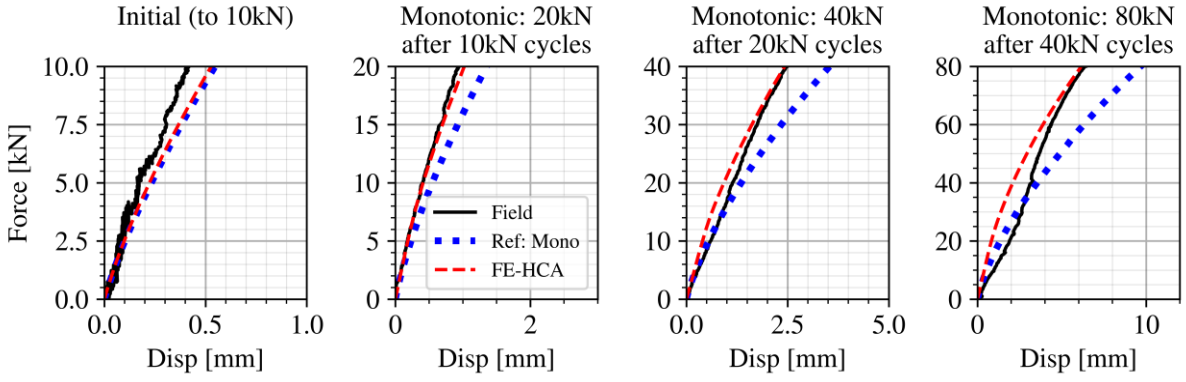


Figure 18 Increases in pile initial stiffness due to cyclic load packages.

While full drainage applied at Dunkirk (matching the field pile dimensions, loading rate and water table depth), excess pore pressures could build up in other cases. Piezometer measurements made offshore over three years in sand at two depths around a 5m diameter (L/D = 5.9) monopile in the Belgian North Sea identified excess pore pressure accumulation during storms and immediately after rotor-stop events. However, excess pressures dissipated rapidly and were negligible under most operational conditions (Stuyts et al., 2023). The present approach can capture, when appropriate, such pore pressure trends at the single element (Figure 12) and field level by re-engaging the low-cycle model regularly (Staubach & Wichtmann, 2020).

7 Conclusions

A rigorous means of undertaking cyclic lateral loading design analyses for piles driven in sands using finite element software is presented by coupling the well-established high-cycle accumulation (HCA) framework with a practice-oriented low-cycle constitutive model and making modifications to ensure numerical robustness and a good fit with laboratory data. The proposed approach, by making consistent each step in the calibration procedure from single element to boundary value problem, allows low-cycle and high-cycle analyses of a wide range of geotechnical boundary value problems taking due account of the cyclic history.

The numerical model, calibrated to high-quality element laboratory tests with a single set of parameters, matched well with the measured accumulated deformation and tilt from instrumented field-scale pile tests carried out at Dunkirk for the PISA joint industry project. The model allowed an examination of how the ground state evolves during cyclic loading, capturing quantitatively the overall stiffening of the pile observed to be a consequence of re-distributed stresses locked-in after cyclic loading. This approach works well to model the cyclic response of field-scale geotechnical structures, validated for cyclic loads in the order of 10^4 cycles with magnitudes of up to 40% of the ultimate monotonic capacity.

8 Acknowledgements

The numerical studies carried out during the first author's doctoral research were funded by the Skempton scholarship from the Civil and Environmental Engineering Department at Imperial College London. The laboratory experiments were carried out as part of the fourth author's doctoral research at the Geotechnical Laboratory of Imperial College London and were partly funded by Ørsted through a post-PISA experimental project. Financial and technical contributions of sponsors and colleagues of the PISA joint industry project are gratefully acknowledged for enabling the field tests presented.

9 References

Abadie, C.N., Beuckelaers, W.J.A.P., Byrne, B.W., Houlsby, G.T., Burd, H.J. & McAdam, R. (2023) Modeling Lifetime Performance of Monopile Foundations for Offshore Wind Applications. *Journal of Geotechnical and Geoenvironmental Engineering*. 149 (8), 04023051. doi:10.1061/JGGEFK.GTENG-9833.

Achmus, M., Kuo, Y.-S. & Abdel-Rahman, K. (2009) Behavior of monopile foundations under cyclic lateral load. *Computers and Geotechnics*. 36 (5), 725–735. doi:10.1016/j.compgeo.2008.12.003.

Aghakouchak, A. (2015) *Advanced laboratory studies to explore the axial cyclic behaviour of driven piles*. PhD. Imperial College London.

Andersen, K.H., Puech, A. & Jardine, R.J. (2013) Cyclic resistant geotechnical design and parameter selection for offshore engineering and other applications. In: A. Puech (ed.). *Proceedings of TC 209 Workshop 18th ICSMGE, Paris 4 September 2013, Design for cyclic loading: piles and other foundations*. 2013 Paris. pp. 9–44. https://htc.issmge.org/uploads/contributions/Andersen_etal(2013).pdf.

ASTM (2023) *Practices for Cycle Counting in Fatigue Analysis*. doi:10.1520/E1049-85R23.

Baldi, G., Bellotti, R., Ghionna, V., Jamiolkowski, M., Marchetti, S. & Pasquelini, E. (1986) Flat dilatometer tests in calibration chambers. In: S.P. Clemence (ed.). *Use of in situ tests in geotechnical engineering*. Geotechnical Special Publication no. 6. New York, NY, USA, American Society of Civil Engineers. pp. 431–446.

Been, K. & Jefferies, M.G. (1985) A state parameter for sands. *Géotechnique*. 35 (2), 99–112. doi:10.1680/geot.1985.35.2.99.

Bentley Systems (2024) *PLAXIS 3D 2024.1: 2 - Reference Manual*. https://bentleysystems.service-now.com/sys_attachment.do?sys_id=a32f2e7a97668a1081d373b0f053afad.

Birrell, M., Pastén, C., Abell, J.A. & Astroza, R. (2022) Probabilistic characterization of a high-cycle accumulation model for sands. *Computers and Geotechnics*. 147, 104798. doi:10.1016/j.compgeo.2022.104798.

Burd, H.J., Beuckelaers, W.J.A.P., Byrne, B.W., Gavin, K.G., Houlsby, G.T., Igoe, D.J.P., Jardine, R.J., Martin, C.M., McAdam, R.A., Muir Wood, A., Potts, D.M., Skov Gretlund, J., Taborda, D.M.G. & Zdravkovic, L. (2020a) New data analysis methods for instrumented medium-scale monopile field tests. *Géotechnique*. 70 (11), 961–969. doi:10.1680/jgeot.18.PISA.002.

Burd, H.J., Taborda, D.M.G., Zdravkovic, L., Abadie, C.N., Byrne, B.W., Houlsby, G.T., Gavin, K.G., Igoe, D.J.P., Jardine, R.J., Martin, C.M., McAdam, R.A., Pedro, A.M.G. & Potts, D.M. (2020b) PISA design model for monopiles for offshore wind turbines: application to a marine sand. *Géotechnique*. 70 (11), 1048–1066. doi:10.1680/jgeot.18.P.277.

Byrne, B.W., McAdam, R.A., Beuckelaers, W.J.A.P., Burd, H.J., Gavin, K., Houlsby, G.T., Igoe, D.J.P., Jardine, R.J., Martin, C.M., Potts, D.M., Taborda, D.M.G. & Zdravkovic, L. (2020) Cyclic laterally loaded medium scale field pile testing for the PISA project. In: *Proceedings of the Fourth International Symposium on Frontiers in Offshore Geotechnics*. 2020 Austin, Texas, U.S. pp. 1323–1331.

CFMS (2020) *Recommendations for planning and designing foundations of offshore wind turbines version 2.1*. Version 2.1. Comite Francais de Mecanique des Soils et de Geotechnique.

Chong, S.-H. & Santamarina, J.C. (2016) Sands subjected to repetitive vertical loading under zero lateral strain: accumulation models, terminal densities, and settlement. *Canadian Geotechnical Journal*. 53 (12), 2039–2046. doi:10.1139/cgj-2016-0032.

Chow, F.C. (1997) *Investigations into the behaviour of displacement piles for offshore foundations*. PhD. Imperial College London.

Collins, I.F. & Boulbibane, M. (2000) Geomechanical Analysis of Unbound Pavements Based on Shakedown Theory. *Journal of Geotechnical and Geoenvironmental Engineering*. 126 (1), 50–59. doi:10.1061/(ASCE)1090-0241(2000)126:1(50).

Corciulo, S., Zanoli, O. & Pisanò, F. (2017) Transient response of offshore wind turbines on monopiles in sand: role of cyclic hydro–mechanical soil behaviour. *Computers and Geotechnics*. 83, 221–238. doi:10.1016/j.compgeo.2016.11.010.

DNV (2021) *DNV-2021-ST-0126 Support structures for wind turbines*.

Galindo, R., Illueca, M. & Jimenez, R. (2014) Permanent deformation estimates of dynamic equipment foundations: Application to a gas turbine in granular soils. *Soil Dynamics and Earthquake Engineering*. 63, 8–18. doi:10.1016/j.soildyn.2014.03.002.

Gao, Z., Yan, L. & Whyte, S. (2023) B-SDM: A bounding surface stiffness degradation method for modelling the long-term ratcheting response of offshore wind turbine foundations. *Computers and Geotechnics*. 154, 105157. doi:10.1016/j.compgeo.2022.105157.

586 Hardin, B.O. & Richart, F.E. (1963) Elastic Wave Velocities in Granular Soils. *Journal of the*
587 *Soil Mechanics and Foundations Division*. 89 (1), 33–65. doi:10.1061/JSFEAQ.0000493.

588 Holland, J.H. (1992) Genetic Algorithms. *Scientific American*. 267 (1), 66–73.

589 Jostad, H.P., Dahl, B.M., Page, A., Sivasithamparam, N. & Sturm, H. (2020) Evaluation of soil
590 models for improved design of offshore wind turbine foundations in dense sand.
591 *Géotechnique*. 70 (8), 682–699. doi:10.1680/jgeot.19.TI.034.

592 Kementzetzidis, E., Pisanò, F. & Metrikine, A.V. (2022) A memory-enhanced p-y model for
593 piles in sand accounting for cyclic ratcheting and gapping effects. *Computers and*
594 *Geotechnics*. 148, 104810. doi:10.1016/j.compgeo.2022.104810.

595 Kheffache, A., Stuyts, B., Jurado, C.S., Weijtjens, W. & Devriendt, C. (2023) Coupled
596 simulations of a monitored wind turbine monopile subject to lateral loading. In:
597 *Proceedings of the 9th International Offshore Site Investigation and Geotechnics Conference*.
598 2023 pp. 1067–1074.

599 Knittel, L., Lamparter, A., Niemunis, A. & Stutz, H.H. (2023) The high-cyclic model for sand
600 tested beyond the usual ranges of application. *Acta Geotechnica*. doi:10.1007/s11440-
601 023-02031-y.

602 Kulhawy, F.H. & Mayne, P.W. (1990) *Manual on estimating soil properties for foundation*
603 *design*.

604 Kuwano, R. (1999) *The stiffness and yielding anistropy of sand*. PhD. Imperial College
605 London.

606 Li, Z., Liu, H., Hicks, M.A. & Pisanò, F. (2023) Influence of static–cyclic load misalignment
607 on the drained tilting response of offshore monopiles in sand. *Computers and Geotechnics*.
608 156, 105306. doi:10.1016/j.compgeo.2023.105306.

609 Liu, H. & Kaynia, A.M. (2023) Characteristics of cyclic undrained model SANISAND-MSu
610 and their effects on response of monopiles for offshore wind structures. *Géotechnique*. 73
611 (4), 281–373. doi:10.1680/jgeot.21.00068.

612 Liu, H.Y., Kementzetzidis, E., Antontio Abell, J. & Pisanò, F. (2022a) From cyclic sand
613 ratcheting to tilt accumulation of offshore monopiles 3D FE modelling using SANISAND-
614 MS. *Géotechnique*. 72 (9), 753–768.

615 Liu, T. (2018) *Advanced laboratory testing for offshore pile foundations under monotonic*
616 *and cyclic loading*. PhD. Imperial College London.

617 Liu, T., Jardine, R.J., Vinck, K. & Ackerley, S.K. (2022b) Optimization of Advanced
618 Laboratory Monotonic and Cyclic Triaxial Testing on Fine Sands. *Geotechnical Testing*
619 *Journal*. 45 (6), 1087–1107. doi:10.1520/GTJ20210190.

620 Lopez-Querol, S. & Coop, M.R. (2012) Drained cyclic behaviour of loose Dogs Bay sand.
621 *Geotechnique*. 62 (4), 281–289. doi:10.1680/geot.8.P.105.

Machacek, J., Wichtmann, T., Zachert, H. & Triantafyllidis, Th. (2018) Long-term settlements of a ship lock: Measurements vs. FE-prediction using a high cycle accumulation model. *Computers and Geotechnics*. 97, 222–232. doi:10.1016/j.compgeo.2018.01.009.

McAdam, R.A., Byrne, B.W., Houlsby, G.T., Beuckelaers, W.J.A.P., Burd, H.J., Gavin, K.G., Igoe, D.J.P., Jardine, R.J., Martin, C.M., Muir Wood, A., Potts, D.M., Skov Gretlund, J., Taborda, D.M.G. & Zdravkovic, L. (2020) Monotonic laterally loaded pile testing in a dense marine sand at Dunkirk. *Géotechnique*. 70 (11), 986–998. doi:10.1680/jgeot.18.PISA.004.

Narsilio, G.A. & Santamarina, J.C. (2008) Terminal densities. *Geotechnique Technical Note*. 58 (8), 669–674. doi:10.1680/geot.2008.58.8.669.

Niemunis, A. & Herle, I. (1997) Hypoplastic model for cohesionless soils with elastic strain range. *Mechanics of Cohesive-frictional Materials*. 2 (4), 279–299. doi:10.1002/(SICI)1099-1484(199710)2:4<279::AID-CFM29>3.0.CO;2-8.

Niemunis, A., Wichtmann, T. & Triantafyllidis, Th. (2005) A high-cycle accumulation model for sand. *Computers and Geotechnics*. 32 (4), 245–263. doi:10.1016/j.compgeo.2005.03.002.

Page, A.M., Klinkvort, R.T., Bayton, S., Zhang, Y. & Jostad, H.P. (2021) A procedure for predicting the permanent rotation of monopiles in sand supporting offshore wind turbines. *Marine Structures*. 75, 102813. doi:10.1016/j.marstruc.2020.102813.

Pasten, C., Shin, H. & Santamarina, J.C. (2014) Long-Term Foundation Response to Repetitive Loading. *Journal of Geotechnical and Geoenvironmental Engineering*. 140 (4), 04013036. doi:10.1061/(ASCE)GT.1943-5606.0001052.

Peralta, P., Ballard, J.C., Rattley, M. & Erbrich, C.E. (2017) Dynamic and cyclic pile-soil response curves for monopile design. In: *Proceedings of the 8th International Conference for Offshore Site Investigation and Geotechnics*. 2017 pp. 1054–1061.

Ruiz López, A. (2024) IC MAGE GenAlgo - Genetic algorithms for geotechnics (Version 1.0). *Zenodo*. doi:10.5281/zenodo.13998194.

Staubach, P. (2022) *Contributions to numerical modelling of pile installation processes and high cyclic loading of soils*. PhD. Ruhr-Universitat Bochum.

Staubach, P., Knittel, L. & Wichtmann, T. (2024) Complex High-Cyclic Loading in an Accumulation Model for Sand. *International Journal for Numerical and Analytical Methods in Geomechanics*. nag.3871. doi:10.1002/nag.3871.

Staubach, P., Machacek, J., Tafili, M. & Wichtmann, T. (2022a) A high-cycle accumulation model for clay and its application to monopile foundations. *Acta Geotechnica*. 17 (3), 677–698. doi:10.1007/s11440-021-01446-9.

Staubach, P., Machacek, J., Tschirschky, L. & Wichtmann, T. (2022b) Enhancement of a high-cycle accumulation model by an adaptive strain. *International Journal for Numerical and Analytical Methods in Geomechanics*. 46, 315–338. doi:10.1002/nag.3301.

660 Staubach, P. & Wichtmann, T. (2020) Long-term deformations of monopile foundations
661 for offshore wind turbines studied with a high-cycle accumulation model. *Computers and*
662 *Geotechnics*. 124, 103553. doi:10.1016/j.compgeo.2020.103553.

663 Stuyts, B., Weijtjens, W., Gkougkoudi-Papaioannou, M., Devriendt, C., Troch, P. &
664 Kheffache, A. (2023) Insights from in-situ pore pressure monitoring around a wind
665 turbine monopile. *Ocean Engineering*. 269, 113556.
666 doi:10.1016/j.oceaneng.2022.113556.

667 Suiker, A.S.J. & De Borst, R. (2003) A numerical model for the cyclic deterioration of
668 railway tracks. *International Journal for Numerical Methods in Engineering*. 57 (4), 441–
669 470. doi:10.1002/nme.683.

670 Taborda, D.M.G. (2011) *Development of Constitutive Models for Application in Soil*
671 *Dynamics*. Imperial College London.

672 Taborda, D.M.G., Pedro, A.M.G., Kontoe, S. & Tsiampousi, A. (2023) IC MAGE Model 02 –
673 Simple state-parameter dependent model with isotropic small strain stiffness (Version
674 2.6). *Zenodo*. doi:10.5281/zenodo.7629677.

675 Taborda, D.M.G., Pedro, A.M.G. & Pirrone, A.I. (2022) A state parameter-dependent
676 constitutive model for sands based on the Mohr-Coulomb failure criterion. *Computers and*
677 *Geotechnics*. 148, 104811. doi:10.1016/j.compgeo.2022.104811.

678 Taborda, D.M.G., Potts, D.M. & Zdravkovic, L. (2016) On the assessment of energy
679 dissipated through hysteresis in finite element analysis. *Computers and Geotechnics*. 71,
680 180–194. doi:10.1016/j.compgeo.2015.09.001.

681 Taborda, D.M.G. & Zdravkovic, L. (2012) Application of a Hill-Climbing technique to the
682 formulation of a new cyclic nonlinear elastic constitutive model. *Computers and*
683 *Geotechnics*. 43, 80–91. doi:10.1016/j.compgeo.2012.02.001.

684 Taborda, D.M.G., Zdravkovic, L., Potts, D.M., Burd, H.J., Byrne, B.W., Gavin, K.G., Houlsby,
685 G.T., Jardine, R.J., Liu, T., Martin, C.M. & McAdam, R.A. (2020) Finite-element modelling of
686 laterally loaded piles in a dense marine sand at Dunkirk. *Géotechnique*. 70 (11), 1014–
687 1029. doi:10.1680/jgeot.18.PISA.006.

688 Tantivangphaisal, P., Taborda, D.M.G. & Kontoe, S. (2024) IC MAGE Model 15 – Simple
689 state-parameter dependent model with isotropic nonlinear stiffness extended with the
690 high-cycle accumulation modelling framework for sands (Version 1.0). *Zenodo*.
691 doi:10.5281/zenodo.14230758.

692 Tantivangphaisal, P., Taborda, D.M.G. & Kontoe, S. (2025) Implementation of a practical
693 sand constitutive model coupled with the High Cycle Accumulation framework in PLAXIS.
694 *MethodsX*. 14, 103183. doi:10.1016/j.mex.2025.103183.

695 Teng, Y., Jostad, H.P. & Zhang, Y. (2018) Experience of Parameter Optimization of the
696 High-Cycle Accumulation Model for Undrained Triaxial Tests on Sand. In: W. Wu & H.-S.
697 Yu (eds.). *Proceedings of China-Europe Conference on Geotechnical Engineering*. Springer
698 Series in Geomechanics and Geoengineering. 2018 Cham, Springer International
699 Publishing. pp. 84–88. doi:10.1007/978-3-319-97112-4_19.

Westermann, K., Zachert, H. & Wichtmann, T. (2014) Vergleich von Ansätzen zur Prognose der Langzeitverformungen von OWEA-Monopilegründungen in Sand Teil 1: Grundlagen der Ansätze und Parameterkalibration. *Bautechnik*. 91 (5), 309–323.

Wichtmann, T. (2005) *Explicit accumulation model for non cohesive soils under cyclic loading*. PhD. Ruhr-Universitat Bochum. https://www.torsten-wichtmann.de/dissertation/dissertation_wichtmann_englisch.pdf.

Wichtmann, T. (2016) *Soil behaviour under cyclic loading - experimental observations constitutive description and applications*. Habilitation. https://www.torsten-wichtmann.de/habil/habil-wichtmann-2016.pdf.

Wichtmann, T. & Knittel, L. (2020) Behaviour of Granular Soils Under Uni- and Multidimensional Drained High-Cyclic Loading. In: T. Triantafyllidis (ed.). *Recent Developments of Soil Mechanics and Geotechnics in Theory and Practice*. Lecture Notes in Applied and Computational Mechanics. Cham, Springer International Publishing. pp. 136–165. doi:10.1007/978-3-030-28516-6_8.

Wichtmann, T., Niemunis, A. & Triantafyllidis, T. (2015) Improved simplified calibration procedure for a high-cycle accumulation model. *Soil Dynamics and Earthquake Engineering*. 70, 118–132. doi:10.1016/j.soildyn.2014.12.011.

Wichtmann, T., Niemunis, A. & Triantafyllidis, T. (2013) On the "elastic stiffness" in a high-cycle accumulation model — continued investigations. *Canadian Geotechnical Journal*. 50 (12), 1260–1272. doi:10.1139/cgj-2013-0037.

Wichtmann, T., Niemunis, A. & Triantafyllidis, T. (2010a) On the "elastic" stiffness in a high-cycle accumulation model for sand: a comparison of drained and undrained cyclic triaxial tests. *Canadian Geotechnical Journal*. 47 (7), 791–805. doi:10.1139/T09-142.

Wichtmann, T., Niemunis, A. & Triantafyllidis, T. (2010b) Strain accumulation in sand due to drained cyclic loading: On the effect of monotonic and cyclic preloading (Miner's rule). *Soil Dynamics and Earthquake Engineering*. 30 (8), 736–745. doi:10.1016/j.soildyn.2010.03.004.

Wichtmann, T., Niemunis, A. & Triantafyllidis, Th. (2007) On the influence of the polarization and the shape of the strain loop on strain accumulation in sand under high-cyclic loading. *Soil Dynamics and Earthquake Engineering*. 27 (1), 14–28. doi:10.1016/j.soildyn.2006.05.002.

Wichtmann, T. & Triantafyllidis, T. (2017) Strain accumulation due to packages of cycles with varying amplitude and/or average stress – On the bundling of cycles and the loss of the cyclic preloading memory. *Soil Dynamics and Earthquake Engineering*. 101, 250–263. doi:10.1016/j.soildyn.2017.07.012.

Williams, S.A., Pelecanos, L. & Darby, A.P. (2022) A practical two-parameter model of pile–soil gapping for prediction of monopile offshore wind turbine dynamics. *Géotechnique*. 1–16. doi:10.1680/jgeot.21.00260.

738 von Wolffersdorff, P.A. (1996) A hypoplastic relation for granular materials with a
739 predefined limit state surface. *Mechanics of Cohesive-frictional Materials*. 1 (3), 251–271.
740 doi:10.1002/(SICI)1099-1484(199607)1:3<251::AID-CFM13>3.0.CO;2-3.

741 Zachert, H., Wichtmann, T., Kudella, P. & Triantafyllidis, T. (2020) Inspection of a high-
742 cycle accumulation model for sand based on recalculations of a full-scale test on a gravity
743 base foundation for offshore wind turbines. *Computers and Geotechnics*. 126, 103727.
744 doi:10.1016/j.compgeo.2020.103727.

745 Zachert, H., Wichtmann, T., Triantafyllidis, T. & Hartwig, U. (2015) Simulation of a full-
746 scale test on a gravity base foundation for offshore wind turbines using a high cycle
747 accumulation model. In: V. Meyer (ed.). *Frontiers in Offshore Geotechnics III*. CRC Press. pp.
748 819–824. doi:10.1201/b18442-115.

749 Zdravkovic, L., Jardine, R.J., Taborda, D.M.G., Abadias, D., Burd, H.J., Byrne, B.W., Gavin, K.G.,
750 Houlsby, G.T., Igoe, D.J.P., Liu, T., Martin, C.M., McAdam, R.A., Muir Wood, A., Potts, D.M.,
751 Skov Gretlund, J. & Ushev, E. (2020) Ground characterisation for PISA pile testing and
752 analysis. *Géotechnique*. 70 (11), 945–960. doi:10.1680/jgeot.18.PISA.001.

753 Zhang, Y., Andersen, K.H., Jeanjean, P., Karlsrud, K. & Haugen, T. (2020) Validation of
754 Monotonic and Cyclic p-y Framework by Lateral Pile Load Tests in Stiff, Overconsolidated
755 Clay at the Haga Site. *Journal of Geotechnical and Geoenvironmental Engineering*. 146 (9),
756 04020080. doi:10.1061/(ASCE)GT.1943-5606.0002318.

757

A. Low-cycle model

Appendix Table A-1 Summary of low-cycle model.

	Model equations	Parameters	State variables
Elastic stiffness at very small strains			
(A.1)	$G_{max} = G_{ref}\frac{(2.17-e)^2}{1+e}\left(\frac{p'}{101.3\ [kPa]}\right)^{m_G};\ K_{max} = \frac{2G_{max}(1+\nu)}{3(1-2\nu)}$	G_{ref}, m_G, ν	e, p'
Critical state line and definition of the Been & Jefferies (1985) sand state-parameter			
(A.2)	$e_{cs} = e_{cs,ref} - \lambda\left(\frac{p'}{101.3\ [kPa]}\right)^{\xi};\ \psi_p = e_p - e_{cs}$	e_{ref}, λ, ξ	e_p, p'
Yield surface			
(A.3)	$J - p'\cdot\left(\frac{\sin(\phi'_{str})}{\cos(\theta)+\sin(\phi'_{str})\frac{\sin(\theta)}{\sqrt{3}}}\right) = 0$ $\phi'_{str} = \arcsin\left(\frac{3M_{str}}{6+M_{str}}\right);\ M_{str} = \frac{6\sin(\phi'_{cs})}{3-\sin(\phi'_{cs})} + k_1\cdot\langle-\psi_p\rangle$	ϕ'_{cs}, k	p', J, θ
Derivatives of the non-associative plastic potential			
(A.4)	$\left\{\frac{\partial P}{\partial p'}, \frac{\partial P}{\partial J}, \frac{\partial P}{\partial \theta}\right\}^T = \left\{-\frac{\sin(\nu_{dil})}{\cos(\theta)+\sin(\nu_{dil})\frac{\sin(\theta)}{\sqrt{3}}},\ 1,\ -p'\frac{\sin(\phi'_{str})}{\cos(\theta)+\sin(\phi'_{str})\cdot\frac{\sin(\theta)}{\sqrt{3}}}\frac{\sin(\theta)-\sin(\nu_{dil})\frac{\cos(\theta)}{\sqrt{3}}}{\cos(\theta)+\sin(\nu_{dil})\frac{\sin(\theta)}{\sqrt{3}}}\right\}^T$ $\nu_{dil} = \arcsin\left(\frac{3M_{dil}}{6+M_{dil}}\right);\ M_{dil} = \min\left(l\cdot\psi_p, 0\right)$	l	e, p', θ
Tangent shear stiffness degradation			
(A.5)	$G_{tan} = G_{max}\left(R_{min} + \frac{1-R_{min}}{\left(1+\left(\frac{E^*_d}{n\cdot a}\right)\right)^b}\right)$	a, b, R_{min}	E^*_d, n $n \in \{1,2\}$
State variable	Hardening law		
p', J, θ	Constitutive relationships in equation (1) and (2)		
e	$\Delta e = -(1+e_0)\cdot\Delta\varepsilon_{vol}$		(A.6)
e_p	$\Delta e_p = -(1+e_0)\cdot\Delta\varepsilon^{pl}_{vol}$		(A.7)
e_0 is the specified initial void ratio.			

B. Modelled construction and loading sequence for pile DM2

Appendix table B-1 Summary of calculation sequence of the medium pile high-cycle lateral load test.

Phase *i*, in calculation order	Constitutive response	Phase type	Applied load boundary condition [kN]**	Δ*N*	Begins from end of phase *i*
1	Low-cycle	Irregular	0-10-0-5	1	-
2		Recording	5-10-0-5	1	1
3	HCA	Accumulation*	5	100	1
4	Low-cycle	Recording (update)	5-10-0-5	300	3
5	HCA	Accumulation	5	300	3
6	Low-cycle	Recording (update)	5-10-0-5	1	5
7	HCA	Accumulation	5	600	5
8	Low-cycle	Recording (update)	5-10-0-5	1	7
9	HCA	Accumulation	5	1500	7
10	Low-cycle	Recording (update)	5-10-0-5	1	9
11	HCA	Accumulation	5	2600	9
12	Low-cycle	Irregular	5-0-20-0-10	1	11
13		Recording	10-20-0-10	1	12
14	HCA	Accumulation*	10	50	12
15	Low-cycle	Recording (update)	10-20-0-10	1	14
16	HCA	Accumulation	10	250	14
17	Low-cycle	Recording (update)	10-20-0-10	1	16
18	HCA	Accumulation	10	800	16
19	Low-cycle	Recording (update)	10-20-0-10	1	18
20	HCA	Accumulation	10	2200	18
21	Low-cycle	Irregular	10-0-40-0-20	1	20
22		Recording	20-40-0-20	1	21
23	HCA	Accumulation*	20	20	21
24	Low-cycle	Recording (update)	20-40-0-20	1	23
25	HCA	Accumulation	20	180	23
26	Low-cycle	Recording (update)	20-40-0-20	1	25
27	HCA	Accumulation	20	800	25
28	Low-cycle	Recording (update)	20-40-0-20	1	27
29	HCA	Accumulation	20	2500	27
30	Low-cycle	Recording (update)	20-40-0-20	1	29

31	HCA	Accumulation	20	4600	29
32	Low-cycle	Irregular	20-0-80-0-40	1	31
33		Recording	40-80-0-40	1	32
34	HCA	Accumulation*	40	10	32
35	Low-cycle	Recording (update)	40-80-0-40	1	34
36	HCA	Accumulation	40	90	34
37	Low-cycle	Recording (update)	40-80-0-40	1	36
38	HCA	Accumulation	40	400	36
39	Low-cycle	Recording (update)	40-80-0-40	1	38
40	HCA	Accumulation	40	800	38
41	Low-cycle	Recording (update)	40-80-0-40	1	40
42	HCA	Accumulation	40	1200	40
43	Low-cycle	Recording (update)	40-80-0-40	1	42
44	HCA	Accumulation	40	2500	42
45	Low-cycle	Recording (update)	40-80-0-40	1	44
46	HCA	Accumulation	40	6100	44

* g_{cyc} is reset at start of phase

** Actual applied load in FE model is halved to take advantage of the symmetric boundary used

764